

Communication

Drone Delivery of Dehydro-Sulfurization Utilizing Doubly-Charged Negative Ions of Nanoscale Catalysts Inspired by the Biomimicry of Bee Species' Bio-Catalysis of Pollen Conversion to Organic Honey

Kelvin L. Suggs¹, Duminda K. Samarakoon² and Alfred Z. Msezane^{1,*} ¹ Department of Physics and Center for Theoretical Studies of Physical Systems, Clark Atlanta University, Atlanta, GA 30314, USA² Department of Biological and Physical Sciences, Northwestern State University, Natchitoches, LA 71497, USA

* Correspondence: amsezane@cau.edu; Tel.: +1-404-880-8663

Abstract: The sulfur dioxide (SO₂) compound is a primary environmental pollutant worldwide, whereas elemental sulfur (S) is a global commodity possessing a variety of industrial as well as commercial functions. The chemical relationship between poisonous SO₂ and commercially viable elemental S has motivated this investigation using the Density Functional Theory calculation of the relative transition state barriers for the two-step dehydro-sulfurization oxidation–reduction reaction. Additionally, doubly-charged nanoscale platelet molybdenum disulfide (MoS₂), armchair (6,6) carbon nanotube, 28-atom graphene nanoflake (GR-28), and fullerene C-60 are utilized as catalysts. The optimal heterogeneous and homogeneous catalysis pathways of the two-step oxidation–reduction from SO₂ to elemental S are further inspired by the biomimicry of the honeybee species' multi-step bio-catalysis of pollen conversion to organic honey. Potential applications include environmental depollution, the mining of elemental sulfur, and the functionalization of novel technologies such as the recently patented aerial and amphibious LynchpinTM drones.

Keywords: fullerene; graphene; molybdenum disulfide; carbon nanotubes; catalysts; density functional theory; enzymes; honeybee biomimicry; drones; depollution; doubly-charged negative ions



Citation: Suggs, K.L.; Samarakoon, D.K.; Msezane, A.Z. Drone Delivery of Dehydro-Sulfurization Utilizing Doubly-Charged Negative Ions of Nanoscale Catalysts Inspired by the Biomimicry of Bee Species' Bio-Catalysis of Pollen Conversion to Organic Honey. *Hydrogen* **2023**, *4*, 133–145. <https://doi.org/10.3390/hydrogen4010009>

Academic Editors: Jan Janczak and Subramanyan Vasudevan

Received: 25 September 2022

Revised: 9 January 2023

Accepted: 23 January 2023

Published: 2 February 2023



Copyright: © 2023 by the authors. Licensee MDPI, Basel, Switzerland. This article is an open access article distributed under the terms and conditions of the Creative Commons Attribution (CC BY) license (<https://creativecommons.org/licenses/by/4.0/>).

1. Introduction

Environmental depollution and mineral synthesis continue to be areas of international interest, given the dynamics of an ever-changing analog-to-digital-to-cloud economy, developing and maintaining sustainable green industrial processes, and future pandemic avoidance [1]. Specifically, elemental S synthesis and SO₂ reduction reactions remain integral to present and future commercial applications and adherence to clean environmental protocols [2,3]. Herein, we use Density Functional Theory to investigate the two-step dehydro-sulfurization reaction. The oxidation–reduction for this two-step reaction entails increased water molecules between steps one and two, with the product of elemental S remaining as the final solute and molecular water remaining as the solvent within the resulting solution. Therefore, the reaction can efficiently serve a two-fold function, namely as an environmental cleaning agent, while simultaneously creating the commercially profitable elemental S as shown by equations 1 and 2 [4,5].

It has previously been predicted and demonstrated that the application of the muon-catalyzed fusion concept is efficient in tuning chemical reaction barriers due to orbital distortion that accelerates reaction bond breakage. Hence, in this work, we extend the muon-catalyzed fusion concept by applying double-charged negative ions to nanoscale molecules that also have been previously shown to be efficacious for tuning chemical reactions [6–8]. Transition metals such as gold, palladium, and silver have been shown previously to be highly

inert in the bulk scale. In this theoretical work, we overcome the tendency for the typical chemical inert behavior of the transition metals by investigating semi-metallic and metallic systems at the nanoscale versus bulk scale and exciting the nanoscale catalysts by an electrical charge equivalent to two negative charges. The introduction of doubly-charged negative ions results in single and double bond breakage in the transition state (TS) and bond reformation in the final state or product in the desulfurization redox reaction [9–11]. Hence, we show the intrinsic value of optimizing the two-step dehydro-sulfurization reaction by the addition of two negative charges to the catalysts molybdenum disulfide, graphene-nanoflake (GR-28), (6,6) armchair carbon nanotube, and fullerene (C-60) [12]. The varying of homogeneous and heterogeneous nanoscale catalysts in each of the two steps of the dehydro-sulfurization reaction is motivated by the novel biomimicry of the fundamental role that the four different enzymes invertase, amylase, glucose oxidase, and catalase play in the bio-catalysis of sucrose conversion to organic honey. We further propose that this study may have future applications in the realm of aero-amphibious drone natural resource mining technologies [13–17].

2. Results

The calculations predict the chemical tunability of two-step transition state paths of the doubly-charged heterogenous and homogenous nanoscale catalysts for the potential application to toxic SO₂ purification systems. As shown in Tables 1 and 2, we report step 1 transition state (TS-1) values of 4.44 eV, 1.12 eV, 0.49 eV, and 0.44 eV for CNT (6,6), MoS₂, GR-28, and C-60, respectively. The step 2 transition state (TS-2) values were 4.36 eV, 1.06 eV, 4.59 eV, and 4.30 eV for CNT (6,6), MoS₂, GR-28, and C-60, respectively. The introduction of doubly-charged negative ions to the dehydro-sulfurization reaction tunes the transition state reaction barriers of metallic and semi-metallic catalysts yielding calculation results that are consistent with previous international academic and commercial findings [18,19]. Figure 1 predicts that each step of the two-step ORR is optimizable via the sequential heterogenous or homogenous utilization of the doubly-charged negative planar catalysts GR-28 for TS-1 and MoS₂ for TS-2 with the calculated respective relative optimal values of 0.49 eV and 1.06 eV. However, a similar TS-1 barrier minimization was realized when spherical C-60 and planar MoS₂ were applied sequentially and step-wise with TS-1 and TS-2 predicted to be 0.44 eV and 1.06 eV. Alternatively, catalysis via the homogenous usage of CNT (6,6) was predicted to slow down significantly the reaction speed with values of 4.44 eV and 4.36 eV for TS-1 and TS-2, respectively. The sole use of the heterogeneous catalyst MoS₂ was to minimize the transition states to 1.12 eV for TS-1 and 1.06 eV for TS-2. Some preliminary neutral transition states were identified according to Table 3, which suggests the optimal barrier reductions for step 1 of CNT (6,6) and step 2 of C-60 due to the addition of a negative charge. These calculations support the application of the short-lived ion creation fundamental mechanism to multi-step chemical reactions. The transition state barriers presented here suggest efficacy for reaction barrier optimization or “chemical tuning” for future depollution and elemental S acquisition applications [20–25].

Table 1. Direct comparison of the calculated relative transition state barrier differential heights from initial states ($\Delta TS = TS - \text{initial state}$) for steps 1 and 2 of the oxidation–reduction reaction to atomic sulfur are represented by $\Delta TS-1$ and $\Delta TS-2$ in electron-volts (eV). Armchair (6,6), carbon nanotube (CNT (6,6)), molybdenum disulfide (MoS₂), graphene flake containing 28 atoms (GR-28), and fullerene (C-60) are the doubly-charged catalysts.

Catalyst (Doubly-Charged)	$\Delta TS-1$ (eV)	Barrier (%) Change (TS-1)	$\Delta TS-2$ (eV)	Barrier (%) Change (TS-2)
CNT (6,6)	4.44	92.6	4.36	73.2
MoS ₂	1.12	70.5	1.06	−10.4
GR-28	0.49	32.7	4.59	74.5
C-60	0.44	25	4.30	72.8
Doubly-charged only	0.33	0	1.17	0

Table 2. Calculated relative initial, transition, and final states in electron-volts (eV) of step 1 and step 2 of the desulfurization redox reaction. The relative states have been calibrated to zero for the lowest calculated potentials that were found in step 1 “or” step 2 for armchair (6,6) carbon nanotube, molybdenum disulfide (MoS₂), graphene flake containing 28 atoms (GR-28), and fullerene (C-60) doubly-charged catalysts. The calculations performed without the assistance of a catalyst for Δ TS-1 and Δ TS-2 are presented as (doubly-charged only) for the introduction of $2e^-$.

Catalyst (Doubly-Charged)	Initial 1 (eV)	TS-1 (eV)	Final 1 (eV)	Initial 2 (eV)	TS-2 (eV)	Final 2 (eV)
CNT (6,6)	0	4.44	15.34	8.89	4.36	5.68
MoS ₂	10.09	11.21	10.16	0	1.06	0.95
GR-28	10.62	11.10	7.05	0	4.59	10.29
C-60	0	0.44	2.31	11.92	4.30	9.53
Doubly-charged only	0	0.33	0.31	0.19	1.17	1.09

Table 3. Calculated neutral relative initial, transition, and final states in electron-volts (eV) of step 1 and step 2 of the desulfurization for armchair (6,6) carbon nanotube, molybdenum disulfide (MoS₂), graphene flake containing 28 atoms (GR-28), and fullerene (C-60) neutral molecular catalysts.

Catalyst (Neutral)	TS-1 (eV)	TS-2 (eV)
CNT (6,6)	10.21	-
MoS ₂	0.05	-
GR-28	0.35	-
C-60	0.03	2.37

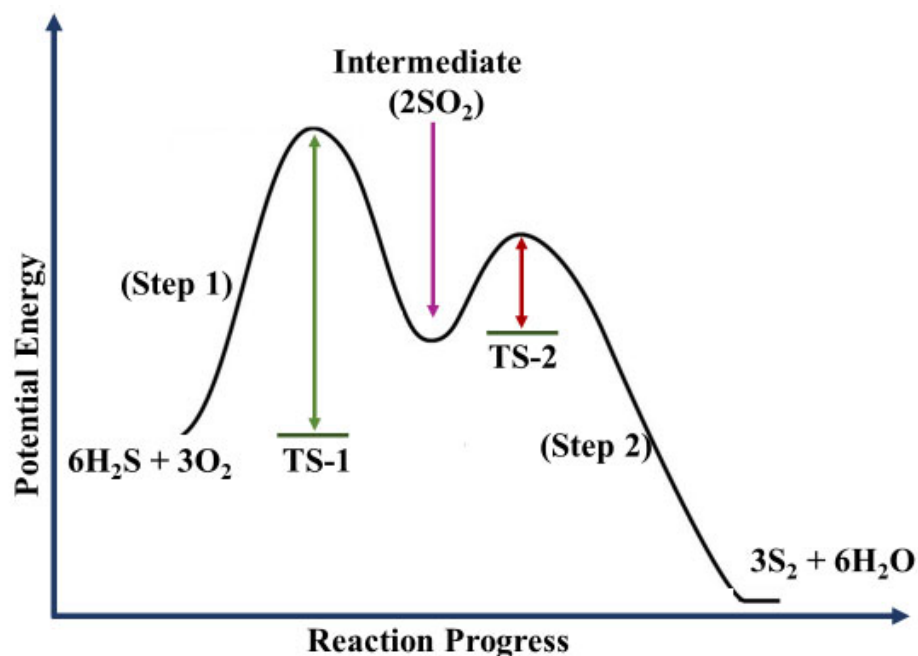


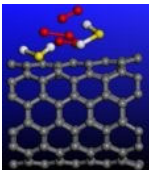
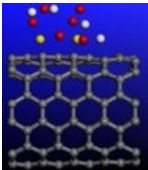
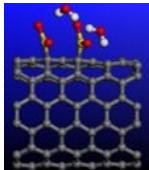
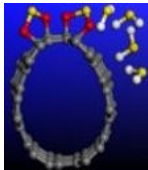
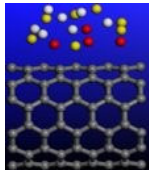

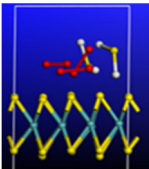
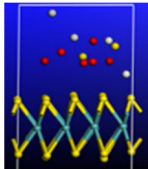
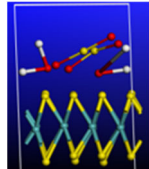
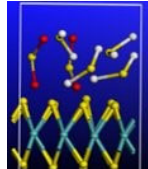
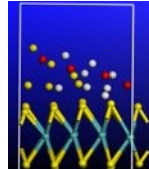
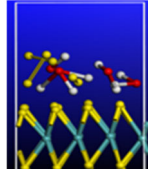
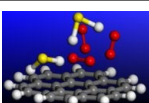
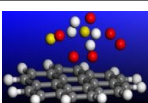
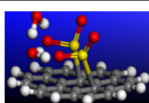
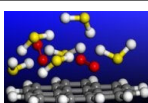
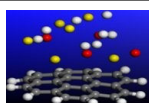
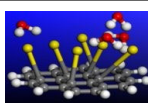
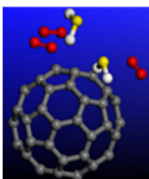
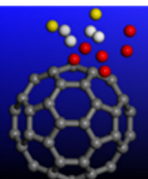
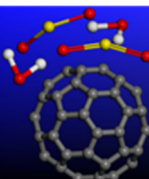
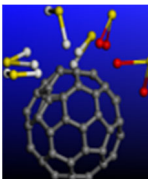
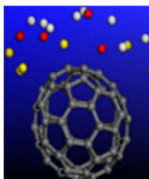
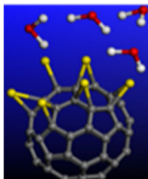
Figure 1. Conceptual rendition of the theoretical two-step transition state reaction path for the dehydro-sulfurization reaction. The black curve indicates net chemical results from Equations (1) and (2) where the activation energies (TS-1) and (TS-2) are the 2-transition state (TS) barriers calculated by Δ TS = TS-initial state for barrier height values for each step represented by the green and dark red arrows respectively. The purple arrow represents the intermediate formation of 2 molar sulfur dioxide.

The desulfurization reaction mechanism may serve as the fundamental process that mimics honeybee bio-catalysis. Moreover, the focus of this work is desulfurization which entails toxic SO_2 elimination with the simultaneous generation of the elemental sulfur commodity rather than organic honey production. It is interesting to note that the mechanism for the biochemical production of honey is documented as an approximated 4-step biocatalytic process involving the four primary enzymes invertase, amylase, glucose oxidase, and catalase [15]. The studied catalysts here are analogously tailored to the two-step desulfurization reaction in lieu of SO_2 elimination, with simultaneous generation of elemental sulfur thereby mimicking the varying of enzymes per each step of the bio-catalysis of organic honey.

3. Discussion

The dehydro-sulfurization reaction is an oxidation–reduction mechanism (ORM), also referred to as a redox reaction. The reactant includes the introduction of diatomic oxygen into sulfur dihydride. Our research approach further introduces two electrons into the chemical reaction in order to increase the catalytic reactivities of heterogeneous (molybdisulfide) MoS_2 as well as the homogeneous molecules armchair (6,6) carbon nanotube, fullerene (C-60), and graphene (Gr-28) as modelled in Table 4.

Table 4. Respective rows of geometrical optimized nanoscale molecules catalyzing the two-step desulfurization reactions. The relative initial, transition, and final state energies are reported in electro-Volts (eV) for the armchair carbon nanotube CNT (6,6), molybdisulfide MoS_2 , 28-atom graphene Gr-28, and fullerene C-60 nanoscale catalysts. The sulfur, carbon, oxygen, and hydrogen atoms are represented by the yellow, gray, red, and white spheres, respectively.

Nanoscale	STEP 1			STEP 2		
Molecules	Initial-1	TS-1	Final-1	Initial-2	TS-2	Final-2
Armchair Carbon Nanotube CNT (6,6)						
Energy Levels	0 eV	4.44 eV	15.34 eV	8.89 eV	4.36 eV	5.68 eV
MoS_2 Molydisulfide						
Energy Levels	10.09 eV	11.21 eV	10.36 eV	0 eV	1.06 eV	0.95 eV
Gr-28 28-atom Graphene						
Energy Levels	10.62 eV	11.10 eV	7.05 eV	0 eV	4.59 eV	10.29 eV
C-60 Fullerene 60						
Energy Levels	0 eV	0.44 eV	2.31 eV	11.92 eV	4.30 eV	9.53 eV

The resulting product is sulfur dioxide precipitated in 2 molar waters due to bond breakage and reformation as indicated by Equation (1). Additionally, two more electrons are added to the catalysts in order to further break the bond arrangements of the reactant in step 2 containing Sulfur dihydride and 2 molar Sulfur dioxide. Hence, the oxygen is removed from the sulfur dioxide due to bond breakage to form 3 molar diatomic sulfurs and 4 molar water in the final product of step 2. The addition of doubly-charged negative ions to the spherical, cylindrical, and planar nanoscale catalysts functions as a “chemical tuning” agent for each step of the dehydro-sulfurization reaction [18–22]. Moreover, the varying of the catalysts with each step of the redox reaction mimics the biocatalytic mechanism of sucrose conversion to organic honey through the flow of $2e^-$ electrons that similarly cause bond breakage and bond reformation occurring in the reaction barriers. The relative barriers generated by the $2e^-$ electrons addition are compared with reference to the initial states according to Equation (3). The two-step chemical reaction can therefore be tailored with various levels of control at each step of the reaction by the sequential application of homogeneous and/or heterogeneous catalysts, as indicated by Figures 1–7. The percentage barrier changes are calculated with Equation (5) and are presented in Table 1, showing that the reaction barriers are increased in Figure 3 by 92.6% and 73.2% for CNT (6,6) calculations of TS-1 and TS-2, respectively. Hence, CNT (6,6) catalysts are predicted to slow the rate of reaction as a substrate for desulfurization. However, MoS₂ is calculated to have a barrier increase of 70.5% for TS-1 and a barrier decrease of –10.2%, as shown in Figure 4, which indicates that MoS₂ is predicted to be an excellent accelerator of reaction for step 2 of desulfurization. Figure 5 illuminates that Gr-28 tends to slow the desulfurization reaction by 32.7% and 74.5% for TS-1 and TS-2, respectively. C-60 is calculated to have the lowest reaction impedance of 25% for step 1, as presented in Figure 6. However, for step 2, the reaction barrier is reported to be 72.8%. Figure 8 shows the respective calculated transition state energies and geometrically optimized view of the catalysis steps when C-60 and MoS₂ catalysts are applied to step 1 and step 2, respectively. The two materials are predicted to effectively maintain or lower transition state barriers when applied sequentially; C-60 changes the barrier by 25%, whereas MoS₂ reduces the transition state energy by –10.4%, according to Table 1. Figures 8–11 are geometrical optimizations of the pollen conversion to the organic honey mechanism that honey bees use, wherefore the enzymes invertase, amylase, glucose oxidase, and catalase are applied in nature for honey production. Similarly, the enzymes are initiated by the flow of $2e^-$; therefore, we have applied two varying inorganic molecules to each step of the reaction rather than applying the catalysts uniformly to all steps. This approach may find efficacy in the optimization to a plethora of other multi-step reactions.

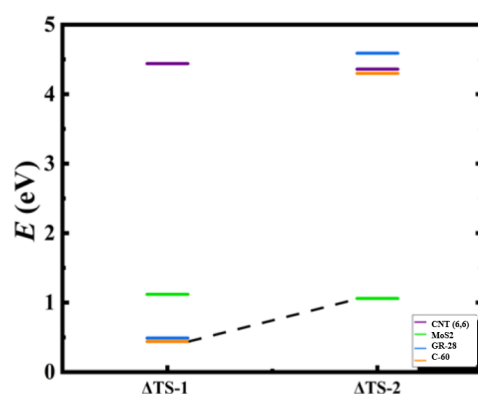


Figure 2. Calculated relative transition state barrier paths values for the two-step Oxidation–Reduction Reaction (ORR) of sulfur dioxide by utilizing armchair (6,6) carbon nanotube, molybdenum disulfide (MoS₂), 28-atomed graphene nanoflake (GR-28), and fullerene (C-60) as catalysts represented by the inset purple, green, blue, and orange bars, respectively. The black dashed line identifies the optimal catalytic path for the transition states 1 and 2. The relative transition state barriers ($\Delta TS-1$) and ($\Delta TS-2$) for the respective steps 1 and 2 are defined by Equation (3): ΔTS = transition state–initial state.

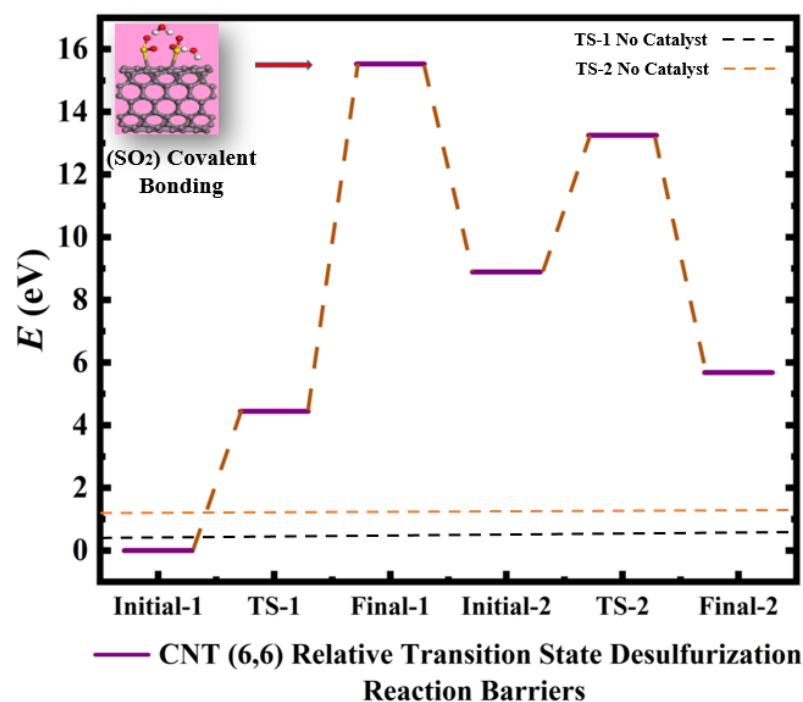


Figure 3. Calculated relative initial, transition, and final states reaction barriers of step 1 and step 2 for the oxidation–reduction of sulfur dioxide to elemental sulfur utilizing armchair carbon nanotube CNT (6,6) represented by the purple bars. Pink Inset: geometrically optimized final state 1 (Final-1) of SO₂ covalently bonding to CNT (6,6) surrounded by two water molecules. Sulfur, carbon, oxygen, and hydrogen are represented by the yellow, gray, red, and white spheres, respectively.

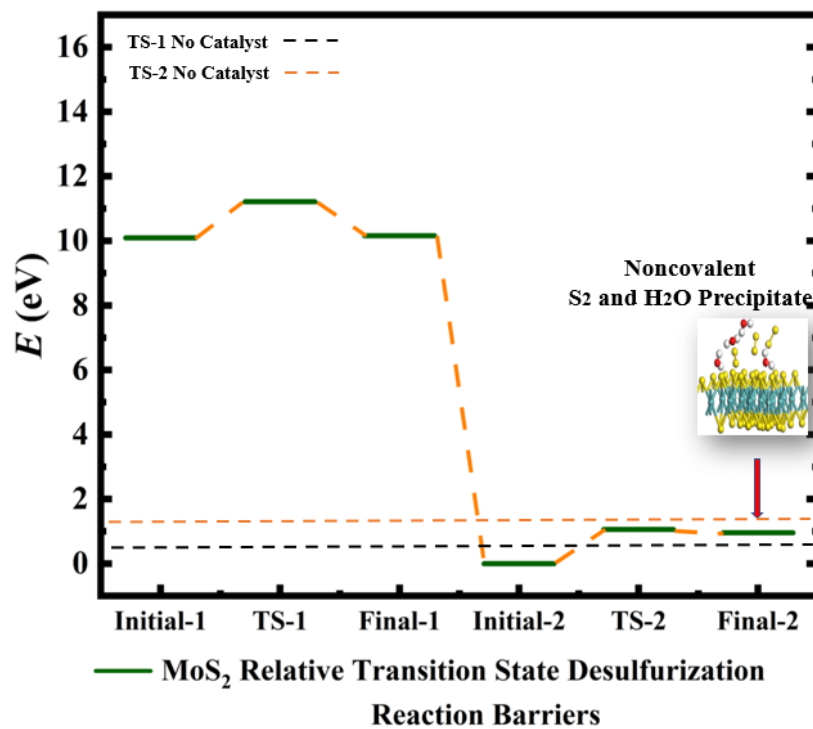


Figure 4. Calculated relative initial, transition, and final states reaction barriers of step 1 and step 2 for the oxidation–reduction of sulfur dioxide to elemental sulfur by utilizing the doubly-charged catalyst MoS₂ represented by the dark green bars. White inset: geometrically optimized final state 2 (Final-2) of MoS₂ with noncovalent precipitated S₂ and H₂O. Sulfur, carbon, oxygen, and hydrogen are represented by the yellow, gray, red, and white spheres, respectively.

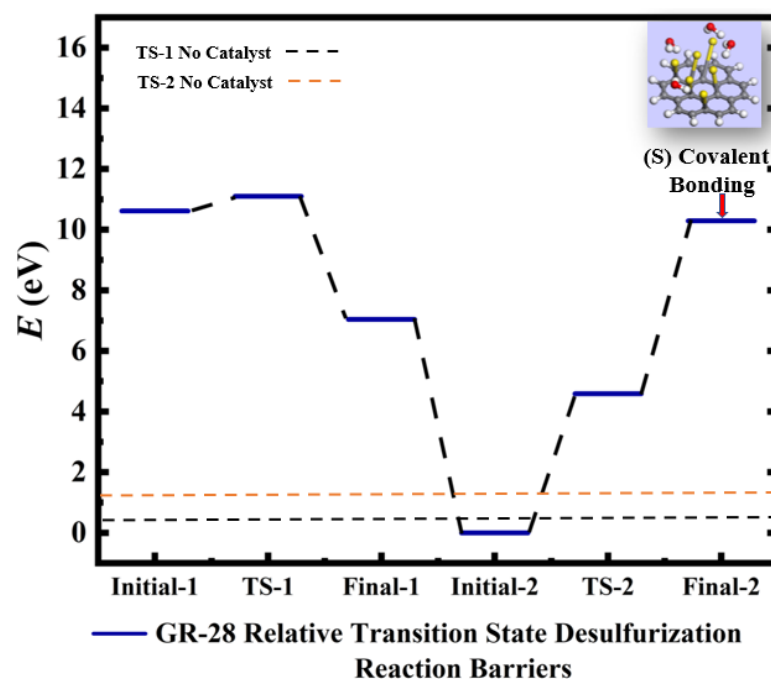


Figure 5. Calculated relative initial, transition, and final states reaction barriers of step 1 and step 2 for the oxidation–reduction of sulfur dioxide to elemental sulfur (S) by utilizing doubly-charged catalyst graphene flake (GR-28) represented by the blue bars. Light blue inset: geometrically optimized final state 2 (Final-2) of GR-28 with covalent bonded atomic S surrounded by 4 molar H_2O . Sulfur, carbon, oxygen, and hydrogen are represented by the yellow, gray, red, and white spheres, respectively.

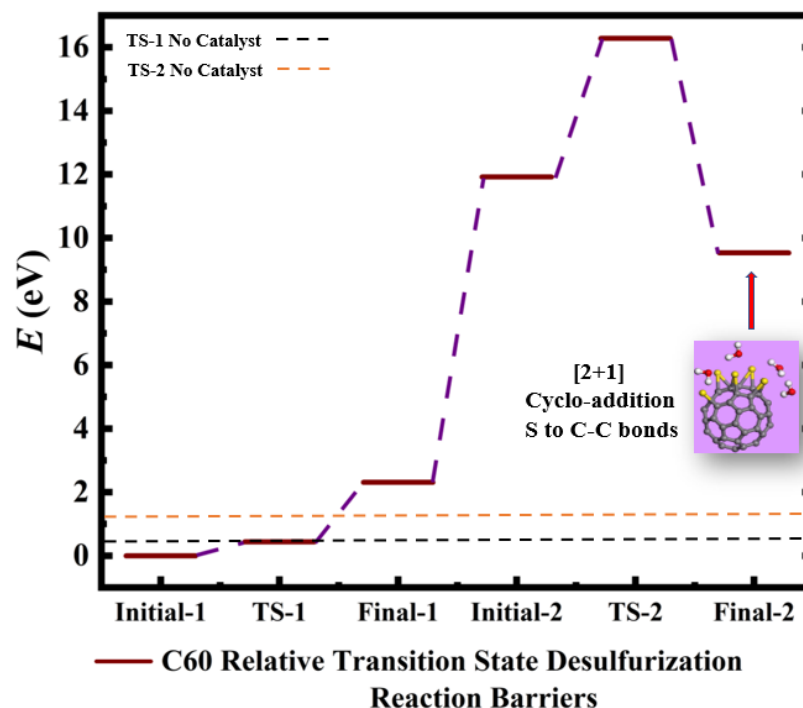


Figure 6. Calculated relative initial, transition, and final states reaction barriers of step 1 and step 2 for the oxidation–reduction of sulfur dioxide to elemental sulfur (S) by utilizing doubly-charged negative fullerene C-60 represented by the brown bars. Light purple inset: geometrically optimized final state 2 (Final-2) of the C-60 catalyst with [2+1] cycloaddition elemental S to fullerene C-C bonds and 4 molar H_2O as the final product for step 2. Sulfur, carbon, oxygen, and hydrogen are represented by the yellow, gray, red, and white spheres, respectively.

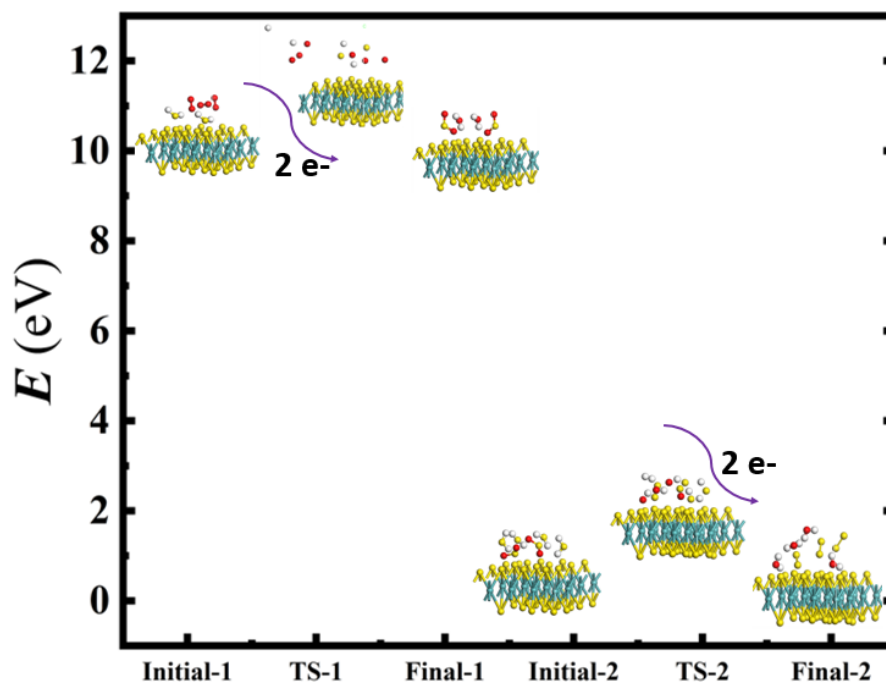


Figure 7. Calculated initial, transition, and final states for geometrically optimized doubly-charged negative AA stacked MoS_2 catalyzing the oxidation–reduction of sulfur dioxide to elemental sulfur. The Mo, S, O, and H atoms are represented by cyan, yellow, red, and white spheres, respectively. The curved arrows demonstrate the introduction of two electrons into the reactant states, causing bond breakage in the predicted transition states of step 1 and step 2, which describes the doubly-charged catalytic process used for our calculations.

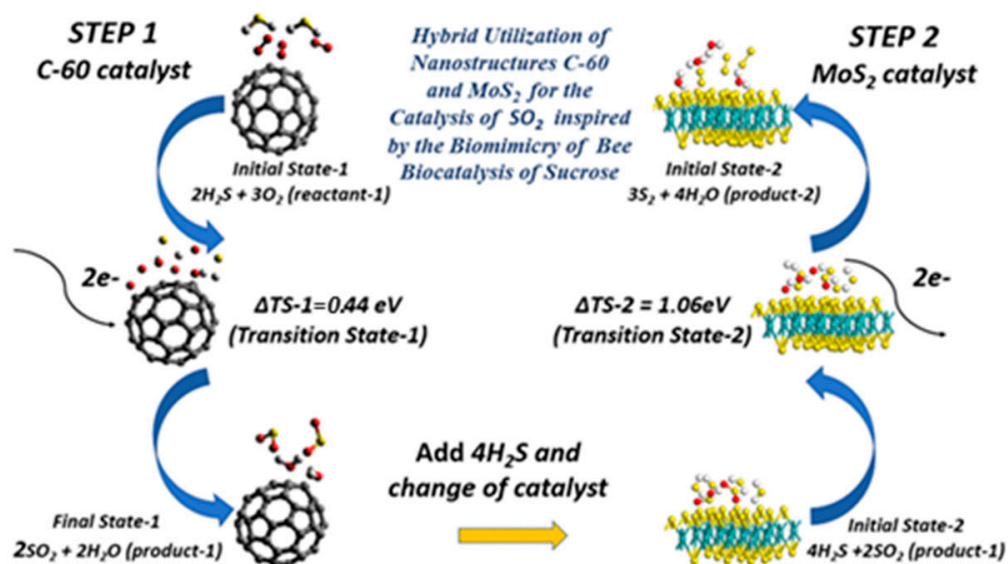


Figure 8. Bee biomimicry inspired rendering of both steps of the initial, transition, and final states for geometrically optimized doubly-charged fullerene C-60 and AA stacked MoS_2 heterogeneously catalyzing the oxidation–reduction of sulfur dioxide to elemental sulfur. The Mo, S, O, and H atoms are represented by cyan, yellow, red, and white spheres, respectively. The curved arrows demonstrate the introduction of two electrons into the reactant states, causing bond breakage in the predicted relative transition states of step 1 and step 2.

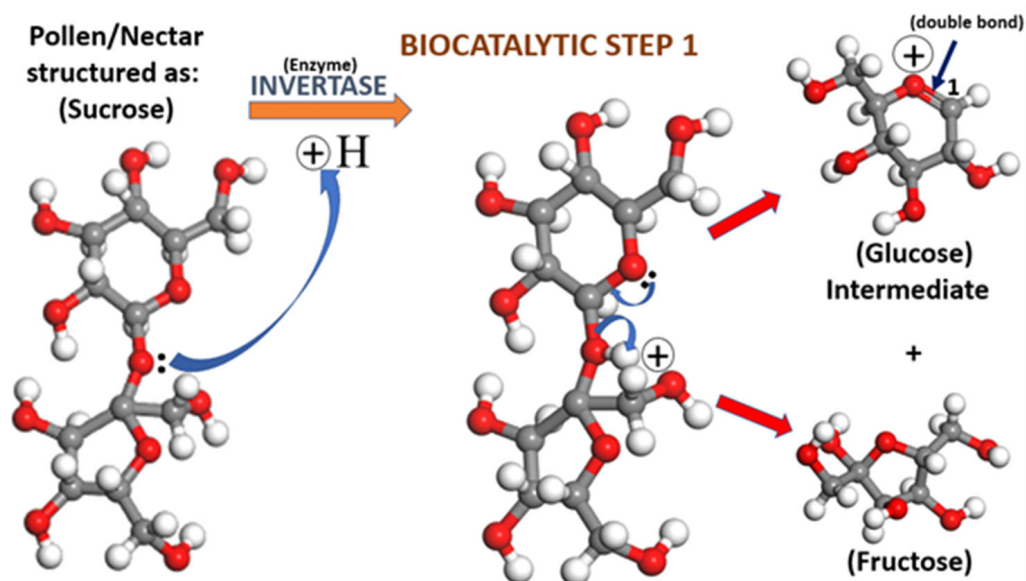


Figure 9. The biocatalytic step 1 conversion of the sucrose molecule ($\text{C}_{12}\text{O}_{11}\text{H}_{22}$) contained in nectar and pollen to intermediate glucose ($\text{C}_6\text{O}_5\text{H}_{11}$) and fructose molecules ($\text{C}_6\text{H}_{12}\text{O}_6$). The orange arrow indicates the utilization of the enzyme invertase as the biocatalytic promoter of the reaction. The blue arrows indicate the flow of two electrons that cause bond breakage and reformation. The gray, red, and white spheres represent carbon, oxygen, and hydrogen, respectively. The red arrows indicate the generation of glucose intermediate and fructose molecules after the application of invertase and bond breakage from sucrose.

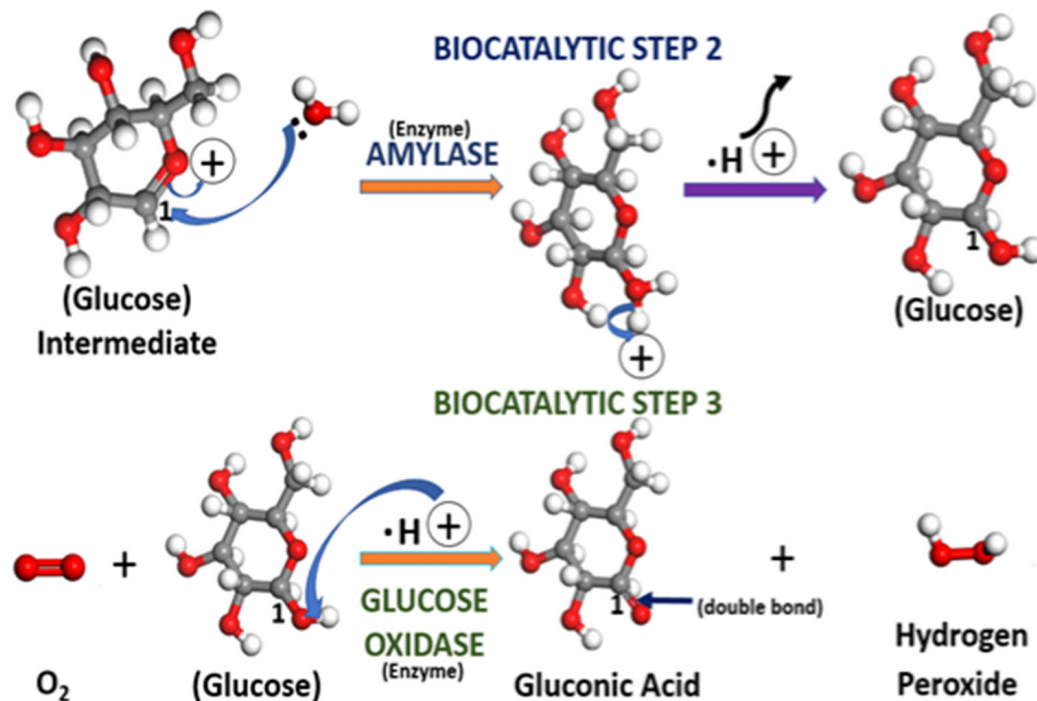


Figure 10. The step 2 and step 3 mechanisms for glucose intermediate decomposition to glucose and the oxidation of glucose ($\text{C}_6\text{H}_{12}\text{O}_6$) to gluconic acid ($\text{C}_6\text{H}_{11}\text{O}_6$) and hydrogen peroxide. Step 2 uses the enzyme amylase, whereas step 3 has the enzyme glucose oxidase as the promotor of the reaction. The index "1" is used to indicate the position of the $\text{C}=\text{O}$ double bond throughout the mechanism. The gray, red, and white spheres represent carbon, oxygen, and hydrogen, respectively.

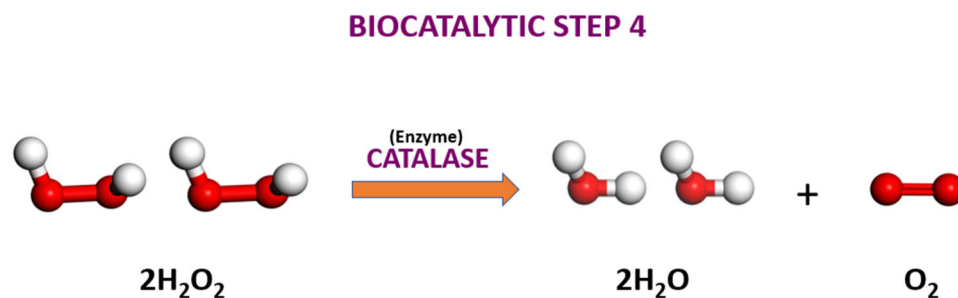
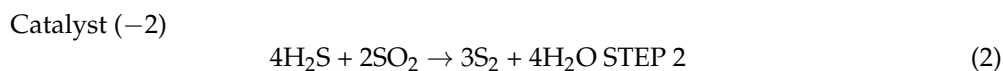
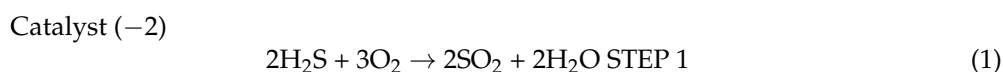


Figure 11. The step 4 of the final step of the sucrose conversion to organic honey. The enzyme catalase decomposes 2 molar hydrogen peroxide to 2 molar water and diatomic oxygen. The red and white spheres represent oxygen and hydrogen, respectively.



$$\Delta\text{TS} = \text{Transition State} - \text{Initial State (Relative T.S. Reaction Barriers)} \quad (4)$$

$$\frac{\text{TS} - \text{std}}{\text{TS}} \times 100\% = (\text{Barrier percentage change given reaction standard}) \quad (5)$$

4. Materials and Methods

[2+1] cyclo-addition is a typical phenomenon that occurs in organo-metallic catalytic systems, oxidation–reduction reactions, and nitrene chemistry. In this work, [2+1] cyclo-addition is specifically used in the geometrical optimization of fullerene C-60, as shown in the inset of Figure 5 [26–28]. However, 28-atomed graphene (GR-28), armchair nanotube (6,6), and MoS₂ catalysts are geometrically optimized by covalent and noncovalent bonding as indicated in the insets of Figures 2–5 and the entirety of Figures 4–6. The doubly-charged MoS₂, GR-28, CNT (6,6), and C-60 catalysis substrates function as reaction barrier tuning mechanisms for the desulfurization oxidation–reduction reaction (ORR), as indicated in Equations (1) and (2) [29,30]. The oxidation–reduction speed is, therefore, predicted to be regulated by the size, type, and charge of any given sample of catalysts used to produce the elemental sulfur and water products for both steps of the reaction. Hence, the quality, quantity, and overall efficiencies of the reactions can be tailored to the reactivity of each step of the ORR reaction, as well as the type of nanoscale catalyst that is used. Transition state theory is executed by performing Density Functional Theory approximations shown to be excellent for predicting chemical, physical, and electromagnetic properties of nanoscopic systems. The initial, transition, and final states are optimized, and are dependent on the application of two negative charges that activate the metallic and semi-metallic planar, cylindrical, and spherical catalysts that cause single and double bond breakage in the transition state consistent with the research findings. The GR-28 nanoflake configuration investigated is due to its similar geometrical structure and chemical function as the “Sulflower” discussed in the 2017 “MOLECULES OF THE YEAR” edition of the *C&EN journal* [30–35]. We use Equation (3) in order to specifically compare the relative transition State (ΔTS) values in Table 1 in order to highlight the most likely efficient heterogenous or homogenous catalyst configuration as indicated in Figure 1 [32–37]. Figures 2–5 show that the calculated relative reaction barriers for the initial, transition, and final states are zeroed to the minimum potential for initial state calculated values occurring in step 1 or step 2 for each set of nanoscale catalysts. A 3-D triclinic lattice type with lattice lengths a:12.7548, b:12.7548, and c:17.2744 Angstroms with subsequent respective angles consisting of α:90, β:90, μ: 120 degrees being used for the AA stacked MoS₂ catalyst. The values of the MoS₂

are represented by a $1 \times 1 \times 1$ Monkhorst–Pack grid, as shown in the inset of Figure 3, as well as the entirety of Figure 6. Noncovalent bonding is used to predict TS-1 and TS-2 for MoS₂ versus the cyclo-addition and covalent approaches utilized for CNT (6,6), GR-28, and C-60. Geometrical optimizations are performed via density functional theory utilizing local density approximation (LDA) with Vosko–Wilk–Nusair (VWN) functional for calculation efficiency. The transition states are calculated by utilizing linear synchronous transit (LST) and quadratic synchronous transit (QST) methods minimum barrier confirmations, as indicated by the data in Table 2, with minimum basis sets and self-consistent field (SCF) tolerances of 0.01 Ha, and smearing values of 0.05 Ha were applied for calculation efficiency consistent with theoretical studies conducted on nanoscale systems and chemical reactions [38,39].

5. Conclusions

The transition states for spherical C-60, planar MoS₂ and graphene (Gr-28), and CNT (6,6) tubal shaped have been calculated. The results indicate efficacy for the chemical tuning of the dehydro-sulfurization reaction as inspired by nature’s biocatalytic solution to the biocatalytic conversion of pollen or nectar to organic honey. We further propose that our findings may assist in the understanding and development of future innovative technologies by utilizing tangential flight-enabled amphibious Lynchpin™ drones as patented and developed by T. Dashawn Howard et al. Some unique capabilities of the patented drone technology include aerial bird-like flocks, bee swarms, and “schools” of fish biomimicry that is tailorable to future multidisciplinary engineering solutions. For example, we postulate that the implementation of our doubly-charged negative-ion catalytic desulfurization predictions combined with the Lynchpin™ drone design may offer promising SO₂ depollution remedies as well as the profitable commercial mining of elemental sulfur [40]. Moreover, the calculations provide some insight into the effects of negative charge on nanoscale systems, as evidenced by recent experimental desulfurization reaction optimizations [41,42].

Author Contributions: K.L.S., D.K.S. and A.Z.M. designed the project and directed it. All authors have read and agreed to the published version of the manuscript.

Funding: The work was partly supported by US DOE Division of Chemical Sciences, Office of Energy Sciences, Office of Energy Research.

Data Availability Statement: Not applicable.

Conflicts of Interest: The authors declare that they have no known competing financial interests or personal relationships that could have appeared to influence the work reported in this research paper. The authors declare no conflict of interest.

References

1. Hu, Y.-L.; Zhu, H.-R.; Wei, S.H. Single-doped charged gold cluster with highly selective catalytic activity for the reduction of SO₂ by CO: First-principles study. *Chin. Phys. B* **2019**, *28*, 113101. [\[CrossRef\]](#)
2. Liu, D.; Ren, S.; Li, W. SO₂ emissions trading and firm exports in China. *Energy Econ.* **2022**, *109*, 105978. [\[CrossRef\]](#)
3. Likus-Cieřlik, J.; Socha, J.; Gruba, P.; Pietrzykowski, M. The Current State of Environmental Pollution with Sulfur Dioxide (SO₂) in Poland Based on Sulfur Concentration in Scots Pine Needles. *Environ. Pollut.* **2020**, *258*, 113559. [\[CrossRef\]](#) [\[PubMed\]](#)
4. Denis, P.A.; Iribarne, F. New Approach to Accomplish the Covalent Functionalization of Boron Nitride Nanosheets: Cycloaddition Reactions. *J. Phys. Chem. C* **2018**, *122*, 18583–18587. [\[CrossRef\]](#)
5. Denis, P.A.; Iribarne, F. Cycloaddition Reactions between Graphene and Fluorinated Maleimides. *J. Phys. Chem. C* **2017**, *121*, 13218–13222. [\[CrossRef\]](#)
6. Felfli, Z.; Suggs, K.; Nicholas, N.; Msezane, A.Z. Fullerene negative ions: Formation and catalysis. *Int. J. Mol. Sci.* **2020**, *21*, 3159. [\[CrossRef\]](#)
7. Suggs, K.; Kiros, F.; Tesfamichael, A.; Felfli, Z.; Msezane, A.Z. Charge modification of metal atoms: Catalysis of Water to Peroxide. *J. Phys. Conf. Ser.* **2015**, *635*, 052018. [\[CrossRef\]](#)
8. Anbar, M.; Schnitzer, R. Doubly Charged Negative Atomic Ions of Hydrogen. *Science* **1976**, *191*, 463–464. [\[CrossRef\]](#)
9. Wang, Z.; Mi, B. Environmental Applications of 2D Molybdenum Disulfide (MoS₂) Nanosheets. *Environ. Sci. Technol.* **2017**, *51*, 8229–8244. [\[CrossRef\]](#)

10. Kroto, H. The stability of the fullerenes C_n , with $n = 24, 28, 32, 36, 50, 60$ and 70 . *Nature* **1987**, *329*, 529–553. [\[CrossRef\]](#)
11. Moosavi-Khoonsari, E.; Van Ende, M.A.; Jung, I.H. Kinetic simulation of hot metal pretreatment: Desulfurization using powder injection. *Metall. Mater. Trans. B* **2022**, *53*, 981–998. [\[CrossRef\]](#)
12. Suggs, K.; Reuven, D.; Wang, X.-Q. Electronic properties of cycloaddition-functionalized graphene. *J. Phys. Chem. C* **2011**, *115*, 3313–3317. [\[CrossRef\]](#)
13. Dunnington, L.; Nakagawa, M. Fast and safe gas detection from underground coal fire by drone fly over. *Environ. Pollut.* **2017**, *229*, 139–145. [\[CrossRef\]](#)
14. Shahmoradi, J.; Talebi, E.; Roghanchi, P.; Hassanalani, M. A Comprehensive Review of Applications of Drone Technology in the Mining Industry. *Drones* **2020**, *4*, 34. [\[CrossRef\]](#)
15. Riddle, S. The Chemistry of Honey. *Bee Culture the Magazine of America Beekeeping*, 25 July 2016.
16. Jung, D.; Streb, C.; Hartmann, M. Covalent Anchoring of Chloroperoxidase and Glucose Oxidase on the Mesoporous Molecular Sieve SBA-15. *Int. J. Mol. Sci.* **2010**, *11*, 762–778. [\[CrossRef\]](#) [\[PubMed\]](#)
17. Billingsley, E.J.; Ghommam, M.; Vasconcellos, R.; Abdelkefi, A. Biomimicry and Aerodynamic Performance of Multi-Flapping Wing Drones. In Proceedings of the AIAA Scitech 2021 Forum, Virtual, 19–21 January 2021; pp. 11–15. [\[CrossRef\]](#)
18. Xu, C.; Gu, Q.; Li, S.; Ma, J.; Zhou, Y.; Zhang, X.; Jiang, C.; Pham-Huu, C.; Liu, Y. Heteroatom-doped monolithic carbocatalysts with improved sulfur selectivity and impurity tolerance for H_2S selective oxidation. *ACS Catal.* **2021**, *11*, 8591–8604. [\[CrossRef\]](#)
19. Shafiq, I.; Shafique, S.; Akhter, P.; Yang, W.; Hussain, M. Recent developments in alumina supported hydrodesulfurization catalysts for the production of sulfur-free refinery products: A technical review. *Catal. Rev.* **2020**, *64*, 1–86. [\[CrossRef\]](#)
20. Suggs, K.; Msezane, A.Z. Doubly-Charged Negative Ions of Triple-Hybrid Atomic-Metal, Super-benzene, Fullerene, and Nanotube as Novel Catalysts for Clean Air through SO_2 Reduction by CO. *Preprints* **2021**.
21. Ye, R.; James, D.K.; Tour, J.M. Laser-Induced Graphene. *Acc. Chem. Res.* **2018**, *51*, 1609–1620. [\[CrossRef\]](#)
22. Ajayan, P.M.; Tour, J.M. Nanotube composites. *Nature* **2007**, *447*, 1066–1068. [\[CrossRef\]](#)
23. Yang, J.; Chen, J.; Wang, X.; Yang, D.; Zhang, Y.; Wu, Y.; Zhao, Y.; Wang, Y.; Wei, Q.; Wang, R.; et al. Improving oxygen reduction reaction of microbial fuel cell by titanium dioxide attaching to dual metal organic frameworks as cathode. *Bioresour. Technol.* **2022**, *349*, 126851. [\[CrossRef\]](#)
24. Hu, F.; Chen, X.; Tu, Z.; Lu, Z.-H.; Feng, G.; Zhang, R. Graphene aerogel supported Ni for CO_2 hydrogenation to methane. *Ind. Eng. Chem. Res.* **2021**, *60*, 12235–12243. [\[CrossRef\]](#)
25. Jin, C.; Cheng, L.; Feng, G.; Ye, R.; Lu, Z.-H.; Zhang, R.; Yu, X. Adsorption of Transition-Metal Clusters on Graphene and N-Doped Graphene: A DFT Study. *Langmuir* **2022**, *38*, 3694–3710. [\[CrossRef\]](#)
26. Cristol, S.; Paul, J.F.; Payen, E.; Bougeard, D.; Clémendot, S.; Hutschka, F. Theoretical study of the MoS_2 (100) surface: A chemical potential analysis of sulfur and hydrogen coverage. *J. Phys. Chem. B* **2000**, *104*, 11220–11229. [\[CrossRef\]](#)
27. Li, Y.; Yang, Y.; Li, K.; Sun, X.; Wang, F.; Hao, Y.; Ning, P.; Wang, C. Theoretical analysis of selective catalytic oxidation of H_2S on $Fe-N_3$ co-doped graphene. *Mol. Catal.* **2022**, *524*, 112318. [\[CrossRef\]](#)
28. Wang, H.; Chen, L.; Lv, Y.; Liu, J.; Feng, G. A First Principle Comparative Study on Chemisorption of H_2 on C_{60} , C_{80} , and $Sc_3N@C_{80}$ in Gas Phase and Chemisorption of H_2 on Solid Phase C_{60} . *J. Nanomater.* **2014**, *2014*, 676908. [\[CrossRef\]](#)
29. Chen, X.; Ge, F.; Lai, N. Probing the catalytic activity and poisoning-tolerance ability of endohedral metallofullerene $Fe_n@C_{60}$ ($n = 1-7$) catalysts in the oxygen reduction reaction. *J. Electrochem. Soc.* **2020**, *167*, 024515. [\[CrossRef\]](#)
30. Ritter, S.K. MOLECULES OF THE YEAR C&EN highlights some of the coolest compounds reported in 2017: “A New Sulflower Bloomed”. *C EN* **2017**, *95*, 2–29.
31. Dong, R.; Pfeffermann, M.; Skidin, D.; Wang, F.; Fu, Y.; Narita, A.; Tommasini, M.; Moresco, F.; Cuniberti, G.; Berger, R.; et al. Persulfurated Coronene: A New Generation of “Sulflower”. *J. Am. Chem. Soc.* **2017**, *139*, 2168–2171. [\[CrossRef\]](#)
32. Karatas, O.; Gengec, N.A.; Gengec, E.; Khataee, A.; Kobya, M. High-performance carbon black electrode for oxygen reduction reaction and oxidation of atrazine by electro-Fenton process. *Chemosphere* **2021**, *287*, 132370. [\[CrossRef\]](#)
33. Xu, F.; Cai, S.; Lin, B.; Yang, L.; Le, H.; Mu, S. Geometric Engineering of Porous PtCu Nanotubes with Ultrahigh Methanol Oxidation and Oxygen Reduction Capability. *Small* **2022**, *18*, 2107387. [\[CrossRef\]](#)
34. Betiha, M.A.; Rabie, A.M.; Ahmed, H.S.; Abdelrahman, A.A.; El-Shahat, M.F. Oxidative desulfurization using graphene and its composites for fuel containing thiophene and its derivatives: An update review. *Egypt. J. Pet.* **2018**, *27*, 715–730. [\[CrossRef\]](#)
35. Gómez-Martínez, M.; Buxaderas, E.; Pastor, I.M.; Alonso, D.A. Palladium nanoparticles supported on graphene and reduced graphene oxide as efficient recyclable catalyst for the Suzuki-Miyaura reaction of potassium aryltrifluoroborates. *J. Mol. Catal. A Chem.* **2015**, *404*–*405*, 1–7. [\[CrossRef\]](#)
36. Maihom, T.; Sittiwong, J.; Probst, M.; Limtrakul, J. Understanding the interactions between lithium polysulfides and anchoring materials in advanced lithium–sulfur batteries using density functional theory. *Phys. Chem. Chem. Phys.* **2022**, *24*, 8604–8623. [\[CrossRef\]](#) [\[PubMed\]](#)
37. Liao, X.; Lu, R.; Xia, L.; Liu, Q.; Wang, H.; Zhao, K.; Wang, Z.; Zhao, Y. Density Functional Theory for Electrocatalysis. *Energy Environ. Mater.* **2022**, *5*, 157–185. [\[CrossRef\]](#)
38. Wang, B.; Jin, C.; Shao, S.; Yue, Y.; Zhang, Y.; Wang, S.; Chang, R.; Zhang, H.; Zhao, J.; Li, X. Electron-deficient Cu site catalyzed acetylene hydrochlorination. *Green Energy Environ.* **2022**; in press. [\[CrossRef\]](#)
39. Delley, B. An all-electron numerical method for solving the local density functional for polyatomic molecules. *J. Chem. Phys.* **1990**, *92*, 508–517. [\[CrossRef\]](#)

40. Delley, B. From molecules to solids with the DMol3 approach. *J. Chem. Phys.* **2000**, *113*, 7756–7764. [[CrossRef](#)]
41. Howard, T.D. Systems and Methods for Lynchpin Structure Applications. US Patent 11117065, 28 July 2022. Available online: <https://patents.justia.com/patent/11117065> (accessed on 15 September 2022).
42. Lou, M.; Bao, J.L.; Zhou, L.; Naidu, G.N.; Robatjazi, H.; Bayles, A.I.; Everitt, H.O.; Nordlander, P.; Carter, E.A.; Halas, N.J. Direct H₂S Decomposition by Plasmonic Photocatalysis: Efficient Remediation plus Sustainable Hydrogen Production. *ACS Energy Lett.* **2022**, *7*, 3666–3674. Available online: <https://pubs.acs.org/doi/10.1021/acsenergylett.2c01755#> (accessed on 20 September 2020). [[CrossRef](#)]

Disclaimer/Publisher’s Note: The statements, opinions and data contained in all publications are solely those of the individual author(s) and contributor(s) and not of MDPI and/or the editor(s). MDPI and/or the editor(s) disclaim responsibility for any injury to people or property resulting from any ideas, methods, instructions or products referred to in the content.